The Astrophysical Journal, 968:77 (13pp), 2024 June 20 https://doi.org/10.3847/1538-4357/ad3e69

# Gemini Near Infrared Spectrograph—Distant Quasar Survey: Rest-frame Ultraviolet—Optical Spectral Properties of Broad Absorption Line Quasars

Harum Ahmed[1], Ohad Shemmer[1], Brandon Matthews[1], Cooper Dix[1,2], Trung Ha[1,3], Gordon T. Richards[4], Michael S. Brotherton[5], Adam D. Myers[5], W. N. Brandt[6,7,8], Sarah C. Gallagher[9], Richard Green[10], Paulina Lira[11], Jacob N. McLane[5], Richard M. Plotkin[12,13], and Donald P. Schneider[6,7]

[1] Department of Physics, University of North Texas, Denton, TX 76203, USA; HarumAhmed@my.unt.edu
[2] Department of Astronomy, The University of Texas at Austin, Austin, TX 78712, USA
[3] Center for Computational Astrophysics, Flatiron Institute, 162 Fifth Avenue, New York, NY 10010, USA
[4] Department of Physics, Drexel University, 32 S. 32nd Street, Philadelphia, PA 19104, USA
[5] Department of Physics and Astronomy, University of Wyoming, Laramie, WY 82071, USA
[6] Department of Astronomy and Astrophysics, The Pennsylvania State University, University Park, PA 16802, USA
[7] Institute for Gravitation and the Cosmos, The Pennsylvania State University, University Park, PA 16802, USA
[8] Department of Physics, 104 Davey Lab, The Pennsylvania State University, University Park, PA 16802, USA
[9] Department of Physics & Astronomy, University of Western Ontario, 1151 Richmond Street, London, ON N6C 1T7, Canada
[10] Steward Observatory, University of Arizona, 933 N. Cherry Avenue, Tucson, AZ 85721, USA
[11] Departmento de Astronomìa, Universidad de Chile, Casilla 36D, Santiago, Chile
[12] Department of Physics, University of Nevada, Reno, NV 89557, USA
[13] Nevada Center for Astrophysics, University of Nevada, Las Vegas, NV 89154, USA

*Received 2024 February 2; revised 2024 April 11; accepted 2024 April 12; published 2024 June 13*

## Abstract

We present the rest-frame ultraviolet–optical spectral properties of 65 broad absorption line (BAL) quasars from the Gemini Near Infrared Spectrograph–Distant Quasar Survey (GNIRS-DQS). These properties are compared with those of 195 non-BAL quasars from GNIRS-DQS in order to identify the drivers for the appearance of BALs in quasar spectra. In particular, we compare equivalent widths and velocity widths, as well as velocity offsets from systemic redshifts, of principal emission lines. In spite of the differences between their rest-frame ultraviolet spectra, we find that luminous BAL quasars are generally indistinguishable from their non-BAL counterparts in the rest-frame optical band at redshifts $1.55 \lesssim z \lesssim 3.50$. We do not find any correlation between BAL trough properties and the H$\beta$-based supermassive black hole masses and normalized accretion rates in our sample. Considering the Sloan Digital Sky Survey quasar sample, which includes the GNIRS-DQS sample, we find that a monochromatic luminosity at rest-frame 2500 Å of $\gtrsim 10^{45}$ erg s$^{-1}$ is a necessary condition for launching BAL outflows in quasars. We compare our findings with other BAL quasar samples and discuss the roles that accretion rate and orientation play in the appearance of BAL troughs in quasar spectra.

*Unified Astronomy Thesaurus concepts:* Active galactic nuclei (16); Quasars (1319); Broad-absorption line quasar (183)

## 1. Introduction

Active galaxies are distinguished from quiescent galaxies by the presence of rapidly accreting supermassive black holes (SMBHs) in their centers. The growth of SMBHs over cosmic history appears to be linked to the buildup of their host galaxies, with more massive galaxies generally harboring more massive SMBHs (e.g., Magorrian et al. 1998; Marconi & Hunt 2003; Di Matteo et al. 2005; Yang et al. 2018).

Quasars, the most powerful active galactic nuclei, can affect their host galaxies by displacing gas and also depositing energy in the form of outflows (e.g., Silk & Rees 1998; Cattaneo et al. 2005; Hopkins et al. 2005; Begelman et al. 2006; Hu et al. 2006). Observationally, such outflows are manifested by 10%–15% of luminous quasars showing signatures of broad absorption lines (BALs) in their rest-frame ultraviolet (UV) spectra (e.g., Reichard et al. 2003; Trump et al. 2006; Ganguly et al. 2007b; Knigge et al. 2008; Gibson et al. 2009). These BAL features are typically associated with high-ionization emission lines (HiBALs; e.g., C IV $\lambda$1549, Si IV $\lambda$1393, N V $\lambda$1240) that are generally blueshifted with respect to systemic redshifts ($z_{\rm sys}$), perhaps partly due to outflows from accretion disk winds (e.g., Murray et al. 1995; Richards et al. 2011). Low-ionization BAL quasars (LoBALs; ~10% of the BAL quasar population; e.g., Voit et al. 1993; Trump et al. 2006), on the other hand, are characterized by the presence of additional low-ionization species (e.g., Mg II $\lambda$2803, Al III $\lambda$1857) in their spectra.

Traditionally, BAL quasars have been defined by the presence of BAL troughs with a minimum velocity width of 2000 km s$^{-1}$ at 10% depth below the UV continuum (Weymann et al. 1991, hereafter W91). However, it is important to note that W91 defined this index based on low-resolution and low signal-to-noise ratio (S/N) Large Bright Quasar Survey spectra. As a result, the absence of the BAL designation in lower-quality data does not guarantee that a quasar is not a BAL quasar (see Section 2).

Other common characteristics of BAL quasars include evidence for significant dust reddening of the continuum, extinction in their UV–optical spectra (e.g., Sprayberry & Foltz 1992; Richards et al. 2002; Reichard et al. 2003; Trump et al. 2006), and the fact that the vast majority of BAL quasars appear to have low observed X-ray fluxes, with respect to predicted values, based on their optical fluxes (e.g., Brandt et al. 2000; Luo et al. 2014). While some BAL quasars may be intrinsically X-ray weak, evidence generally suggests that X-ray weakness in these sources is primarily due to obscuration (e.g., Gallagher et al. 2002, 2006; Liu et al. 2018; Wang et al. 2022; but see also Teng et al. 2014; Morabito et al. 2014).

Additionally, the fraction of quasars displaying BALs drops precipitously among the most radio-loud[14] (RL) objects (e.g., Stocke et al. 1992; Brotherton et al. 1998; Becker et al. 2001; Richards et al. 2011). There are indications that this trend may differ for radio-intermediate sources ($10 < R < 100$), where the fraction of BAL quasars increases with radio luminosity (e.g., Petley et al. 2024; but see also Calistro Rivera et al. 2023). BAL features can also introduce $z_{\mathrm{sys}}$ uncertainties; however, masking the locations of these features decreases the redshift errors by about 1% and the number of catastrophic redshift errors by about 80% (e.g., García et al. 2023).

There have been claims that BAL quasars are simply "normal" quasars observed along preferential lines of sight that penetrate outflowing gas (e.g., W91; Ogle et al. 1999; Schmidt & Hines 1999; Elvis 2000; Brotherton et al. 2006; DiPompeo et al. 2012; Rankine et al. 2020, hereafter R20). However, it is also evident that BAL quasars may signify a distinct evolutionary stage, where "evolution" refers to changes in the spectral energy distribution (SED). During this stage, absorbing material with a high covering fraction is expelled from the central regions of the quasar (e.g., Voit et al. 1993; Becker et al. 1997; Gregg et al. 2006; Lípari & Terlevich 2006; Urrutia et al. 2009). R20 further emphasizes that the structure of BALs varies across the observed parameter space, and different SEDs lead to different mean BAL properties. Observationally, careful comparisons of the rest-frame UV emission-line properties reveal that BAL and non-BAL quasars appear to be drawn from the same parent population of quasars (e.g., W91; Reichard et al. 2003; Baskin et al. 2013). In addition, Gallagher et al. (2007) highlight that the mid-infrared properties of BAL quasars are also consistent with those of non-BAL quasars of comparable luminosity.

While in the early studies models were often employed to suggest either orientation or evolution as explanations for BAL properties, it becomes clear that a combination of evolutionary and orientation effects, along with other factors, must contribute to the observed phenomena. Consequently, investigating the underlying physics becomes crucial for a comprehensive understanding of the structure, evolution, and feedback mechanisms among all quasars and their host galaxies.

This paper aims to analyze rest-frame UV–optical spectra of BAL and non-BAL quasars, comparing emission-line properties and velocity offsets from $z_{\mathrm{sys}}$ to shed light on the drivers for the appearance of BALs in quasar spectra. Prior studies, such as those by W91 and Reichard et al. (2003), have delved into similar investigations, examining rest-frame UV spectra between BAL and non-BAL quasars. Our study focuses primarily on comparing rest-frame optical properties between the two groups of quasars. A statistically meaningful comparison of this kind is now possible by utilizing the Gemini Near Infrared Spectrograph−Distant Quasar Survey (GNIRS-DQS), which includes 65 (195) luminous BAL (non-BAL) quasars (Matthews et al. 2021, 2023, hereafter M21, M23, respectively).

The structure of this paper is as follows. In Section 2, the sample selection and methodology are described. Section 3 presents our main results. Section 4 discusses our main findings, with comparisons to other work. Section 5 presents our summary and conclusions. Throughout this work, we adopt a ΛCDM cosmology with $H_0 = 70$ km s$^{-1}$ Mpc$^{-1}$, $\Omega_M = 0.3$, and $\Omega_\Lambda = 0.7$ when calculating quantities such as quasar luminosities or luminosity distances (e.g., Spergel et al. 2007).

## 2. Sample Selection

A prerequisite for any investigation of the statistical distribution of emission-line properties is a large, well-defined source catalog. To investigate differences in the rest-frame optical properties of quasars with BAL features compared to those without, one generally must resort to sources above $z \sim 1.5$. Below that threshold, the scarcity of rest-frame UV spectra poses a challenge, as these spectra are primarily available through the Hubble Space Telescope (HST) archive in a nonuniform fashion and based on numerous selection criteria. Consequently, a more cost-effective approach is to conduct the study at higher redshifts, where uniform catalogs of rest-frame UV spectra are more abundant, and rest-frame optical spectra can be obtained more economically from near-infrared (NIR) spectroscopy.

For this reason, we selected sources from the GNIRS-DQS catalog, which constitutes the largest uniform inventory of rest-frame optical spectral properties of luminous quasars at high redshift from the Sloan Digital Sky Survey (SDSS; York et al. 2000). Specifically, the catalog consists of 260 quasars, 65 of which are BAL quasars, having $-28.0 \lesssim M_i \lesssim -30.0$ mag with redshifts between $1.55 \lesssim z \lesssim 3.50$ (to center the H$\beta$ +[O III] spectral complex in the $J$, $H$, and $K$ bands) with monochromatic luminosities ($\lambda L_\lambda$) at rest-frame 5100 Å (hereafter $\lambda L_{5100}$) in the range of $\sim 10^{46}$–$10^{47}$ erg s$^{-1}$. Our sample consists primarily of HiBAL quasars, with four LoBAL quasars previously identified by Trump et al. (2006) or confirmed through visual inspection. The small number of LoBAL quasars prevents us from conducting a statistically meaningful comparison with their HiBAL counterparts.

The GNIRS-DQS selection criteria may have excluded sources known to exhibit some degree of obscuration. Thus, there is a possibility that a certain number of luminous SDSS BAL quasars did not meet the brightness threshold of GNIRS-DQS. Additionally, there is also a possibility that the GNIRS-DQS sample is biased toward more face-on systems given the high luminosities of these sources (e.g., Runnoe et al. 2013; DiPompeo et al. 2014). Yet, in such a scenario, we would have anticipated a larger fraction of RL quasars and, correspondingly a lower fraction of BAL quasars.

As mentioned in Section 1, RL quasars are a small fraction of the overall quasar population, and this fraction is even lower among BAL quasars. While 17 non-BAL quasars in our sample are formally RL, only one of the BAL quasars, SDSS J114705.24 + 083900.6, is also an RL quasar; in total, RL quasars constitute ∼7% of the entire GNIRS-DQS sample. If our sample is indeed biased toward more face-on systems, correcting for this orientation bias would likely result in a higher BAL quasar fraction than we measure (65/260 = 25%), which is a less probable scenario. Furthermore, we also examine whether our sample is biased with respect to

---

[14] We define radio-loud quasars as sources having radio-loudness values of $R > 100$, where $R$ is the ratio of the flux densities at 5 GHz and 4400 Å (Kellermann et al. 1989).

radio-loudness. This investigation involves analyzing photometric data from the Wide-field Infrared Survey Explorer (WISE; e.g., Wright et al. 2010), specifically focusing on W1 and W2 magnitudes with respect to radio-loudness. We find no discernible differences between BAL and non-BAL quasars, or between RL and non-RL quasars, across the NIR continuum of these sources. Therefore, we do not have evidence that our sample is biased with respect to quasar orientation or radio-loudness.

The spectral measurements in this work were obtained from the catalog of spectroscopic properties of the GNIRS-DQS quasars in M23. M23 determined the $z_{\rm sys}$ values for GNIRS-DQS sources based on the available emission line that carried the smallest intrinsic uncertainty (see Boroson 2005; Shen et al. 2016; Nguyen et al. 2020). In order of increasing uncertainty, these values are obtained from [O III] $\lambda$5007, Mg II $\lambda\lambda$2798, 2803, and H$\beta$ $\lambda$4861. For those objects where [O III] is too weak to obtain a reliable $z_{\rm sys}$ measurement, Mg II and H$\beta$ are substituted as suitable proxies (see M23).

The SMBH masses ($M_{\rm BH}$) and mass-weighted accretion rates (i.e., Eddington ratios, or $L/L_{\rm Edd}$ values) for all sources in this work were obtained from Dix et al. (2023, hereafter D23) and Ha et al. (2023, hereafter H23) following the prescription in Maithil et al. (2022). Briefly, these values are single-epoch $M_{\rm BH}$ estimates using the H$\beta$ line coupled with corrections based on the Fe II emission strength in the rest-frame wavelength range 4434–4684 Å (see Du & Wang 2019).

Rest-frame optical properties for the 65 BAL quasars taken from M23 are reported in Table 1. Column (1) provides the source name; Column (2) gives the redshift based on H$\beta$ ($z_{{\rm H}\beta}$); Column (3) gives the redshift based on [O III] ($z_{\rm [O\,III]}$); Column (4) gives the velocity offset between the two redshifts; Column (5) gives rest-frame equivalent width (EW) of the H$\beta$ line; Column (6) gives rest-frame EW(Fe II); Column (7) gives full-width at half maximum (FWHM) intensity of H$\beta$; Column (8) gives rest-frame EW([O III]); Column (9) gives FWHM([O III]); Column (10) gives asymmetry of [O III] $\lambda$5007; Column (11) gives log $\lambda L_{5100}$; Column (12) gives Fe II–corrected H$\beta$-based $M_{\rm BH}$ estimates taken from D23; Column (13) gives Fe II–corrected H$\beta$-based $L/L_{\rm Edd}$ values taken from H23.

Rest-frame UV properties for the 65 BAL quasars are reported in Table 2. Column (1) provides the source name; Column (2) gives the visually inspected redshift, $z_{\rm vi}$, from SDSS Data Release 16 (DR16, Lyke et al. 2020, Table D1, Column (17)); Column (3) gives the systemic redshift from M23; Column (4) gives the velocity offset between the two redshifts; Column (5) gives the C IV emission-line rest-frame EW from R20 for 52 BAL sources; Column (6) gives C IV blueshifts from R20. Additionally, Column (7) gives the balnicity index (BI), defined by W91 for C IV as

$$\mathrm{BI} = \int_{3000}^{25000} \left(1 - \frac{f(v)}{0.9}\right) C\, dv\ (\mathrm{km\ s^{-1}}), \tag{1}$$

where $f(v)$ is the continuum-normalized flux as a function of velocity, $v$, relative to the line center. The constant $C$ equals 1 in regions where $f(v) < 0.9$ for at least 2000 km s$^{-1}$, counting from large to small outflow velocities; otherwise, $C = 0$. The outflow velocity, $v$, is defined to be negative for blueshifts. BI is the traditionally used metric to separate BAL quasars from their non-BAL counterparts. In addition to BI, Column (8) gives the absorption index (AI), defined by Hall et al. (2002) as

$$\mathrm{AI} = \int_{0}^{25000} \left(1 - \frac{f(v)}{0.9}\right) C\, dv\ (\mathrm{km\ s^{-1}}), \tag{2}$$

to account for uncertainties in the systemic redshift, the continuum shape, and to measure intrinsic absorption systems. Here $C$ equals 1 in regions where $f(v) < 0.9$ continuously for at least 450 km s$^{-1}$. The BI and AI values in Table 2 were obtained from the literature (Column (9)); 11 sources that have no measurable BI values with AI > 0 are marked with BI = 0, two sources have both BI = 0 and AI = 0, and one source with no measurable AI value with BI > 0 is marked with AI = 0 (see Table 2). All these sources have been visually classified as BAL quasars (see M23). Table 3 provides the mean ($\mu$), standard error on the mean (SEM), standard deviation ($\sigma$), and median (Med) with bootstrapped uncertainty estimates for the properties listed in Table 1, as well as the associated probability ($p$-value) of statistical tests (see below) for BAL and non-BAL sources in Columns (2)–(11), respectively.

## 3. Analysis and Results

### 3.1. Rest-frame Optical Properties

We compare basic properties for multiple rest-frame optical emission lines between the 65 BAL and 195 non-BAL sources in GNIRS-DQS in Figure 1. This figure includes a comparison of the rest-frame EWs of the H$\beta$ and [O III] emission lines. The means and medians are consistent within their errors for both distributions (see Table 3). It is evident that at $1.55 \lesssim z \lesssim 3.50$ a large fraction of BAL quasars have [O III] emission that is just as strong as that of the non-BAL quasars in the GNIRS-DQS sample. This result is likely due to a narrow luminosity range inherent in the GNIRS-DQS sample.

By design, GNIRS-DQS targeted highly luminous quasars, biased toward having higher $L/L_{\rm Edd}$ values. The [O III] emission in luminous high-redshift quasars is relatively weak (whether BAL or not, due to the Baldwin effect; Baldwin 1977), and, similarly, Fe II emission is relatively strong in such sources (e.g., Dietrich et al. 2002; Netzer et al. 2004; Shen et al. 2016; M21; M23). At lower redshifts, however, a larger range of parameter space is observed (e.g., a broader range of quasar luminosities).

To check whether the BAL outflows are manifested in the sources' [O III] emission-line properties, we compare the FWHM and asymmetry values of the [O III] $\lambda$5007 emission line (taken from Table 1) between BAL and non-BAL quasars in Figure 1. The mean and median FWHM([O III]), as well as the asymmetry values for BAL and non-BAL quasars, are consistent within their errors (see Table 3). We also computed the velocity offset ($\Delta v$) between the $z_{{\rm H}\beta}$ and $z_{\rm [O\,III]}$ values of a source between BAL and non-BAL quasars, using

$$\Delta v_i = c\left(\frac{z_{{\rm H}\beta} - z_{\rm [O\,III]}}{1 + z_{\rm [O\,III]}}\right) \tag{3}$$

where $c$ is the speed of light in km s$^{-1}$. The distributions of $\Delta v$ values for BAL and non-BAL quasars are presented in Figure 1.

The relative intensity of the Fe II emission blend with respect to the H$\beta$ line appears to be correlated with quasar accretion rate in terms of $L/L_{\rm Edd}$ (e.g., Boroson & Green 1992; Netzer & Trakhtenbrot 2007; Shen & Ho 2014; Du & Wang 2019).

### Table 1
Optical Spectral Properties of 65 BAL Quasars from GNIRS-DQS

| Quasar (SDSS J) | $z_{\mathrm{H}\beta}$ | $z_{[\mathrm{O\,III}]}$ | Velocity Offset (km s$^{-1}$) | $\mathrm{EW}_{\mathrm{H}\beta}$ (Å) | $\mathrm{EW}_{\mathrm{Fe\,II}}$ (Å) | $\mathrm{FWHM}_{\mathrm{H}\beta}$ (km s$^{-1}$) | $\mathrm{EW}_{[\mathrm{O\,III}]}$ (Å) | $\mathrm{FWHM}_{[\mathrm{O\,III}]}$ (km s$^{-1}$) | $\mathrm{Asymmetry}_{[\mathrm{O\,III}]}$ | log $\lambda L_{5100}$ (erg s$^{-1}$) | log $M_{\mathrm{BH}}$ ($M_{\odot}$) | $L/L_{\mathrm{Edd}}$ |
|---|---|---|---|---|---|---|---|---|---|---|---|---|
| 001249.89 + 285552.6 | 3.248 | 3.237 | 807 | $47^{+11}_{-14}$ | $39 \pm 3$ | $4622^{+334}_{-442}$ | $9^{+1}_{-1}$ | $2394^{+1}_{-1}$ | 0.015 | 46.78 | 9.40 | 1.41 |
| 001355.10 − 012304.0 | 3.391 | 3.380 | 793 | $97^{+34}_{-45}$ | $41.7 \pm 0.3$ | $7323^{+1451}_{-1920}$ | $20^{+1}_{-1}$ | $1918^{+1}_{-1}$ | −0.191 | 46.60 | 9.87 | 0.33 |
| 004613.54 + 010425.7 | 2.171 | 2.166 | 392 | $92^{+1}_{-1}$ | $32 \pm 1$ | $3522^{+97}_{-128}$ | $24^{+1}_{-1}$ | $955^{+1}_{-1}$ | −0.039 | 46.48 | 9.21 | 1.14 |
| 013012.36 + 153157.9 | 2.344 | 2.343 | 77 | $64^{+1}_{-2}$ | $18 \pm 1$ | $4734^{+116}_{-153}$ | $15^{+1}_{-1}$ | $778^{+40}_{-52}$ | −0.166 | 46.35 | 9.43 | 0.51 |
| 013652.52 + 122501.5 | 2.394 | 2.388 | 537 | $104^{+2}_{-3}$ | $43 \pm 1$ | $4897^{+1599}_{-2116}$ | $30^{+1}_{-1}$ | $2041^{+1}_{-1}$ | −0.097 | 46.47 | 9.46 | 0.61 |
| 014018.20 − 013805.8 | 2.232 | 2.235 | −319 | $51^{+1}_{-1}$ | $12.9 \pm 0.3$ | $6212^{+129}_{-171}$ | $7^{+1}_{-1}$ | $1138^{+1}_{-1}$ | −0.217 | 46.64 | 9.80 | 0.41 |
| 014206.86 + 025713.0 | 2.323 | 2.325 | −117 | $48^{+2}_{-2}$ | $23 \pm 1$ | $4721^{+86}_{-114}$ | $17^{+1}_{-1}$ | $1496^{+105}_{-139}$ | −0.077 | 46.76 | 9.54 | 0.98 |
| 022007.64 − 010731.1 | 3.436 | 3.429 | 469 | $85^{+2}_{-3}$ | $33.4 \pm 0.1$ | $3867^{+116}_{-154}$ | $19^{+1}_{-1}$ | $2819^{+1}_{-1}$ | 0.108 | 46.62 | 9.33 | 1.16 |
| 025042.45 + 003536.7 | 2.398 | … | … | $122^{+2}_{-3}$ | $28 \pm 1$ | $8886^{+577}_{-763}$ | <1 | … | … | 46.45 | 10.04 | 0.16 |
| 073519.68 + 240104.6 | 3.295 | … | … | $62^{+3}_{-4}$ | $32 \pm 1$ | $5227^{+193}_{-256}$ | <1 | … | … | 46.51 | 9.50 | 0.61 |
| 080636.81 + 345048.5 | 1.548 | 1.547 | 121 | $87^{+29}_{-39}$ | $59 \pm 3$ | $4427^{+653}_{-863}$ | $12^{+2}_{-2}$ | $2936^{+379}_{-501}$ | 0.413 | 46.11 | 9.12 | 0.61 |
| 081114.66 + 172057.4 | 2.341 | 2.341 | −2 | $59^{+1}_{-1}$ | $9.8 \pm 0.5$ | $6841^{+149}_{-196}$ | $17^{+1}_{-1}$ | $1922^{+1}_{-1}$ | −0.436 | 46.49 | 9.85 | 0.26 |
| 083745.74 + 052109.4 | 2.364 | 2.361 | 306 | $71^{+3}_{-4}$ | $30 \pm 1$ | $3950^{+125}_{-165}$ | $22^{+1}_{-1}$ | $2275^{+1}_{-1}$ | −0.149 | 46.31 | 9.20 | 0.78 |
| 084133.15 + 200525.7 | 2.360 | ... | ... | $27^{+1}_{-1}$ | $28 \pm 1$ | $5582^{+143}_{-189}$ | <1 | ... | ... | 47.00 | 9.60 | 1.49 |
| 084401.95 + 050357.9 | 3.358 | 3.341 | 1220 | $50^{+1}_{-1}$ | $19 \pm 1$ | $5964^{+1}_{-1}$ | $43^{+1}_{-1}$ | $5811^{+1}_{-1}$ | −0.042 | 47.19 | 9.97 | 0.97 |
| 084729.52 + 441616.7 | 2.346 | 2.343 | 261 | $71^{+10}_{-13}$ | $30.7 \pm 0.1$ | $4257^{+362}_{-479}$ | $15^{+1}_{-1}$ | $719^{+1}_{-1}$ | 0.143 | 46.37 | 9.29 | 0.73 |
| 085046.17 + 522057.4 | 2.235 | … | … | $59^{+1}_{-1}$ | $36 \pm 2$ | $4445^{+226}_{-298}$ | <1 | … | … | 46.62 | 9.38 | 1.05 |
| 091301.01 + 422344.7 | 2.317 | 2.314 | 309 | $81^{+1}_{-1}$ | $38 \pm 1$ | $4512^{+114}_{-150}$ | $41^{+1}_{-1}$ | $1795^{+1}_{-1}$ | −0.497 | 46.50 | 9.39 | 0.78 |
| 091328.23 + 394443.9[a] | 1.582 | 1.587 | −605 | $39^{+3}_{-4}$ | $45 \pm 4$ | $2543^{+307}_{-406}$ | $11^{+1}_{-1}$ | $1289^{+1}_{-1}$ | −0.019 | 46.02 | 8.44 | 2.41 |
| 091425.72 + 504854.9 | 2.367 | 2.368 | −116 | $64^{+3}_{-4}$ | $45 \pm 1$ | $4584^{+93}_{-123}$ | $8^{+1}_{-1}$ | $1258^{+126}_{-167}$ | −0.384 | 46.32 | 9.24 | 0.74 |
| 091716.79 + 461435.3 | 1.630 | 1.625 | 548 | $19^{+3}_{-4}$ | $1 \pm 1 \times 10^{-7}$ | $5571^{+1569}_{-2076}$ | $31^{+1}_{-1}$ | $778^{+1}_{-1}$ | −0.144 | 46.31 | 9.65 | 0.28 |
| 093251.98 + 023727.0 | 2.172 | 2.171 | 131 | $51^{+1}_{-1}$ | $38 \pm 1$ | $5988^{+113}_{-150}$ | $10^{+1}_{-1}$ | $1917^{+1}_{-1}$ | 0.026 | 46.47 | 9.52 | 0.54 |
| 094328.94 + 140415.6[a] | 2.412 | … | … | $53^{+5}_{-6}$ | $44 \pm 1$ | $5940^{+640}_{-846}$ | <1 | … | … | 46.55 | 9.52 | 0.65 |
| 094427.27 + 614424.6 | 2.338 | 2.340 | −169 | $79^{+2}_{-3}$ | $24 \pm 1$ | $4898^{+2279}_{-3015}$ | $38^{+2}_{-2}$ | $1795^{+186}_{-246}$ | −0.229 | 46.41 | 9.47 | 0.53 |
| 094902.38 + 531241.5 | 1.613 | 1.609 | 430 | $64^{+1}_{-2}$ | $48 \pm 1$ | $4345^{+121}_{-161}$ | $4^{+1}_{-1}$ | $1139^{+1}_{-1}$ | 0.915 | 46.19 | 9.11 | 0.74 |
| 095746.75 + 565800.7 | 1.585 | 1.576 | 1103 | $26^{+4}_{-5}$ | $61 \pm 1$ | $2613^{+364}_{-481}$ | $2^{+1}_{-1}$ | $321^{+1}_{-1}$ | −0.046 | 46.39 | 8.20 | 9.36 |
| 100610.55 + 370513.8 | 3.195 | 3.202 | −490 | $72^{+3}_{-4}$ | $51.2 \pm 1 \times 10^{-16}$ | $5601^{+547}_{-724}$ | $20^{+1}_{-1}$ | $674^{+1}_{-1}$ | −0.238 | 46.78 | 9.61 | 0.87 |
| 100653.26 + 011938.7 | 2.298 | 2.303 | −427 | $62^{+1}_{-2}$ | $46 \pm 1$ | $5850^{+302}_{-400}$ | $21^{+1}_{-1}$ | $1735^{+1}_{-1}$ | −0.408 | 46.40 | 9.47 | 0.52 |
| 101542.04 + 430455.6 | 2.428 | 2.415 | 1115 | $59^{+4}_{-5}$ | $54 \pm 2$ | $3763^{+137}_{-181}$ | $5^{+1}_{-1}$ | $2875^{+194}_{-256}$ | −0.021 | 46.48 | 9.07 | 1.57 |
| 102154.00 + 051646.3 | 3.448 | … | … | $61^{+1}_{-1}$ | $16.5 \pm 0.1$ | $5254^{+226}_{-300}$ | <1 | … | … | 46.70 | 9.68 | 0.63 |
| 103246.19 + 323618.0 | 2.380 | … | … | $36^{+1}_{-1}$ | $37 \pm 1$ | $4755^{+249}_{-330}$ | <1 | … | … | 46.44 | 9.21 | 1.04 |
| 103405.73 + 463545.4 | 2.213 | 2.215 | −203 | $63^{+2}_{-3}$ | $26 \pm 1$ | $6489^{+191}_{-254}$ | $17^{+12}_{-11}$ | $718^{+974}_{-718}$ | −0.665 | 46.44 | 9.69 | 0.34 |
| 103718.23 + 302509.1 | 2.299 | 2.288 | 977 | $100^{+57}_{-76}$ | $40.1 \pm 1 \times 10^{-10}$ | $4724^{+123}_{-163}$ | $26^{+1}_{-1}$ | $3538^{+1}_{-1}$ | 0.033 | 46.39 | 9.40 | 0.60 |
| 104621.57 + 483322.7 | 1.580 | … | … | $39^{+1}_{-2}$ | $60 \pm 3$ | $4222^{+417}_{-552}$ | <1 | … | … | 46.15 | 8.79 | 1.41 |
| 104941.58 + 522348.9 | 2.367 | 2.369 | −115 | $97^{+2}_{-3}$ | $21 \pm 1$ | $5663^{+391}_{-517}$ | $40^{+6}_{-8}$ | $2152^{+595}_{-787}$ | −0.198 | 46.27 | 9.57 | 0.31 |
| 110148.85 + 054815.5 | 1.589 | 1.584 | 600 | $48^{+1}_{-2}$ | $17 \pm 1$ | $7944^{+457}_{-605}$ | $17^{+1}_{-1}$ | $3473^{+249}_{-329}$ | 0.00022 | 46.38 | 9.86 | 0.20 |
| 111313.29 + 102212.4 | 2.261 | … | … | $81^{+1}_{-1}$ | $42 \pm 1$ | $4752^{+144}_{-190}$ | <1 | … | … | 46.58 | 9.45 | 0.81 |
| 111352.53 + 104041.9 | 1.607 | 1.609 | −233 | $26^{+1}_{-2}$ | $5.4 \pm 0.1$ | $6068^{+760}_{-1005}$ | $5^{+1}_{-1}$ | $1675^{+1}_{-1}$ | −0.554 | 46.39 | 9.69 | 0.31 |
| 111920.98 + 232539.4 | 2.288 | 2.289 | −53 | $46^{+1}_{-1}$ | $9.5 \pm 1 \times 10^{-15}$ | $3901^{+126}_{-167}$ | $28^{+1}_{-1}$ | $1557^{+1}_{-1}$ | −0.180 | 46.35 | 9.28 | 0.71 |
| 112127.79 + 254758.9 | 1.602 | 1.602 | −8 | $77^{+1}_{-2}$ | $4.4 \pm 0.2$ | $4700^{+1591}_{-2105}$ | $39^{+1}_{-2}$ | $898^{+77}_{-102}$ | −0.395 | 46.39 | 9.52 | 0.46 |
| 112938.46 + 440325.0 | 2.212 | 2.212 | −1 | $128^{+4}_{-5}$ | $7.1 \pm 0.1$ | $3267^{+117}_{-154}$ | $46^{+4}_{-5}$ | $659^{+118}_{-156}$ | −0.493 | 46.62 | 9.30 | 1.24 |
| 113048.45 + 225206.6 | 2.378 | 2.364 | 1285 | $34^{+11}_{-15}$ | $9.9 \pm 1 \times 10^{-15}$ | $5358^{+213}_{-282}$ | $11^{+19}_{-11}$ | $3119^{+7805}_{-3119}$ | 0.0067 | 46.39 | 9.55 | 0.42 |

**Table 1**
(Continued)

| Quasar (SDSS J) | $z_{\mathrm{H}\beta}$ | $z_{[\mathrm{O\ III}]}$ | Velocity Offset (km $\mathrm{s}^{-1}$) | $\mathrm{EW}_{\mathrm{H}\beta}$ (Å) | $\mathrm{EW}_{\mathrm{Fe\ II}}$ (Å) | $\mathrm{FWHM}_{\mathrm{H}\beta}$ (km $\mathrm{s}^{-1}$) | $\mathrm{EW}_{[\mathrm{O\ III}]}$ (Å) | $\mathrm{FWHM}_{[\mathrm{O\ III}]}$ (km $\mathrm{s}^{-1}$) | $\mathrm{Asymmetry}_{[\mathrm{O\ III}]}$ | log $\lambda L_{5100}$ (erg $\mathrm{s}^{-1}$) | log $M_{\mathrm{BH}}$ ($M_{\odot}$) | $L/L_{\mathrm{Edd}}$ |
|---|---|---|---|---|---|---|---|---|---|---|---|---|
| 113330.17 + 144758.8 | 3.254 | 3.238 | 1158 | $68^{+3}_{-4}$ | 35 ± 2 | $4629^{+188}_{-249}$ | $9^{+2}_{-2}$ | $2158^{+779}_{-1031}$ | −0.00031 | 46.65 | 9.46 | 0.93 |
| 113740.61 + 630256.9 | 2.318 | 2.323 | −493 | $59^{+2}_{-2}$ | 23 ± 1 | $7995^{+311}_{-411}$ | $4^{+1}_{-1}$ | $757^{+1}_{-1}$ | −0.578 | 46.41 | 9.87 | 0.21 |
| 113924.64 + 332436.9 | 2.310 | 2.315 | −396 | $41^{+1}_{-2}$ | 60 ± 2 | $5454^{+434}_{-574}$ | $1.5^{+1}_{-1}$ | $1672^{+1}_{-1}$ | −0.00044 | 46.31 | 9.12 | 0.95 |
| 114323.71 + 193448.0 | 3.358 | 3.350 | 554 | $77^{+1}_{-1}$ | 18 ± 1 | $5003^{+106}_{-140}$ | $40^{+1}_{-1}$ | $2750^{+1}_{-1}$ | −0.202 | 46.78 | 9.69 | 0.74 |
| 114705.24 + 083900.6 | 1.602 | 1.603 | −122 | $51^{+2}_{-2}$ | 4 ± 1 | $4778^{+378}_{-501}$ | $36^{+1}_{-1}$ | $959^{+47}_{-62}$ | −0.345 | 46.51 | 9.58 | 0.51 |
| 114738.35 + 301717.5 | 3.358 | ⋯ | ⋯ | $46^{+3}_{-4}$ | 29 ± 1 | $4430^{+534}_{-707}$ | <1 | ⋯ | ⋯ | 46.74 | 9.42 | 1.23 |
| 115747.99 + 272459.6 | 2.230 | 2.216 | 1276 | $67^{+2}_{-3}$ | 37 ± 2 | $3896^{+238}_{-314}$ | $12^{+1}_{-1}$ | $1288^{+1}_{-1}$ | −0.00079 | 46.63 | 9.29 | 1.33 |
| 133342.56 + 123352.7 | 3.281 | 3.258 | 1650 | $59^{+1}_{-1}$ | 30 ± 1 | $4150^{+143}_{-190}$ | $11^{+1}_{-1}$ | $2645^{+1}_{-1}$ | −0.022 | 46.79 | 9.43 | 1.36 |
| 140058.79 + 260619.4 | 2.366 | 2.363 | 238 | $54^{+1}_{-1}$ | 31 ± 1 | $2898^{+100}_{-132}$ | $10^{+1}_{-1}$ | $1736^{+1}_{-1}$ | −0.450 | 46.40 | 8.92 | 1.85 |
| 141321.05 + 092204.8 | 3.324 | 3.313 | 737 | $69^{+1}_{-2}$ | 22 ± 1 | $4019^{+87}_{-115}$ | $12^{+1}_{-1}$ | $2097^{+139}_{-184}$ | −0.017 | 46.90 | 9.52 | 1.43 |
| 142013.03 + 253403.9 | 2.234 | 2.235 | −130 | $36^{+2}_{-3}$ | 47 ± 2 | $2820^{+173}_{-228}$ | $6^{+6}_{-5}$ | $539^{+9151}_{-539}$ | 0.048 | 46.56 | 8.71 | 4.29 |
| 142500.24 + 494729.2 | 2.261 | ⋯ | ⋯ | $58^{+1}_{-2}$ | 45 ± 2 | $4134^{+128}_{-169}$ | <1 | ⋯ | ⋯ | 46.46 | 9.19 | 1.14 |
| 150205.58 − 024038.5 | 2.210 | 2.192 | 1667 | $52^{+1}_{-2}$ | 31 ± 1 | $4459^{+164}_{-217}$ | $21^{+1}_{-1}$ | $1994^{+1}_{-1}$ | 0.038 | 46.48 | 9.32 | 0.87 |
| 151123.30 + 495101.2 | 2.396 | ⋯ | ⋯ | $47^{+1}_{-1}$ | 55 ± 1 | $6907^{+231}_{-306}$ | <1 | ⋯ | ⋯ | 46.67 | 9.59 | 0.73 |
| 151341.89 + 463002.7[a] | 1.574 | 1.572 | 203 | $51^{+1}_{-2}$ | 33 ± 1 | $3937^{+63}_{-83}$ | $13^{+1}_{-1}$ | $1257^{+1}_{-1}$ | −0.486 | 46.42 | 9.10 | 0.87 |
| 153248.95 + 173900.8 | 2.348 | 2.350 | −181 | $55^{+1}_{-1}$ | 23 ± 1 | $7286^{+328}_{-434}$ | $12^{+1}_{-1}$ | $1377^{+7381}_{-1277}$ | −0.0089 | 46.56 | 9.78 | 0.26 |
| 154550.37 + 554346.2 | 2.164 | 2.159 | 432 | $111^{+4}_{-5}$ | $6.5 \pm 1 \times 10^{-11}$ | $3152^{+1}_{-1}$ | $42^{+1}_{-1}$ | $1137^{+1}_{-1}$ | −0.327 | 46.72 | 9.25 | 1.24 |
| 160207.67 + 380743.0 | 1.592 | 1.581 | 1214 | $65^{+13}_{-17}$ | 29 ± 1 | $7142^{+1856}_{-2455}$ | $24^{+1}_{-1}$ | $2340^{+92}_{-122}$ | 0.541 | 46.72 | 9.89 | 0.40 |
| 160552.97 + 292141.4 | 2.327 | ... | ... | $87^{+3}_{-4}$ | $20.6 \pm 1 \times 10^{-11}$ | $4345^{+169}_{-224}$ | <1 | ... | ... | 46.56 | 9.46 | 0.76 |
| 163125.10 + 174810.0 | 2.185 | 2.180 | 436 | $76^{+2}_{-2}$ | 7.5 ± 0.3 | $5617^{+237}_{-313}$ | $33^{+2}_{-2}$ | $1736^{+196}_{-259}$ | −0.106 | 46.68 | 9.79 | 0.47 |
| 220344.98 + 235729.3[a] | 2.159 | 2.158 | 79 | $76^{+1}_{-1}$ | 14 ± 1 | $6974^{+271}_{-358}$ | $15^{+1}_{-2}$ | $1436^{+690}_{-521}$ | −0.164 | 46.35 | 9.80 | 0.33 |
| 223934.45 − 004707.2 | 2.226 | 2.215 | 1100 | $62^{+1}_{-2}$ | 38 ± 2 | $6179^{+187}_{-247}$ | $11^{+1}_{-1}$ | $1681^{+1}_{-1}$ | 0.103 | 46.49 | 9.60 | 0.47 |
| 225608.48 + 010557.8 | 2.267 | 2.263 | 350 | $61^{+3}_{-4}$ | $33.1 \pm 1 \times 10^{-10}$ | $2830^{+275}_{-363}$ | $12^{+1}_{-1}$ | $3828^{+1}_{-1}$ | −0.235 | 46.41 | 8.92 | 1.90 |

**Note.**

[a] LoBAL quasars identified by Trump et al. (2006) or through visual inspection.

**Table 2**
UV Spectral Properties of 65 BAL Quasars from GNIRS-DQS

| Quasar (SDSS J) | $z_{\rm vi}$[a] | $z_{\rm sys}$ | Velocity Offset (km s$^{-1}$) | EW$_{\rm C\ IV}$[b] (Å) | Blueshift$_{\rm C\ IV}$[b] (km s$^{-1}$) | BI (km s$^{-1}$) | AI (km s$^{-1}$) | BI/AI References[c] |
|---|---|---|---|---|---|---|---|---|
| 001249.89+285552.6 | 3.236 | 3.233 | 213 | 25 | 1582 | 164 | 1924 | 1 |
| 001355.10-012304.0 | ⋯ | 3.380 | ⋯ | 30 | 1370 | 1226 | 1598 | 3 |
| 004613.54+010425.7 | 2.150 | 2.165 | −1422 | 36 | 2264 | 3393 | 7033 | 1 |
| 013012.36+153157.9 | 2.349 | 2.343 | 538 | 15 | 435 | 5 | 2468 | 1 |
| 013652.52+122501.5 | 2.393 | 2.388 | 443 | 68 | 1060 | 5177 | 6130 | 1 |
| 014018.20-013805.8 | 2.235 | 2.236 | −93 | 33 | 1522 | 1091 | 1404 | 1 |
| 014206.86+025713.0 | 2.315 | 2.323 | −722 | 19 | 640 | 40 | 1229 | 3 |
| 022007.64-010731.1 | 3.441 | 3.428 | 881 | 35 | 2127 | 5649 | 8132 | 1 |
| 025042.45+003536.7 | 2.387 | 2.398 | −971 | 42 | 978 | 5336 | 7361 | 1 |
| 073519.68+240104.6 | 3.278 | 3.282 | −280 | 26 | 1865 | 25 | 1983 | 1 |
| 080636.81+345048.5 | ⋯ | 1.549 | ⋯ | ⋯ | ⋯ | 0 | 0 | 5 |
| 081114.66+172057.4 | 2.323 | 2.341 | −1616 | 26 | 1427 | 405 | 2687 | 1 |
| 083745.74+052109.4 | 2.355 | 2.362 | −625 | 42 | 1582 | 385 | 3137 | 1 |
| 084133.15+200525.7 | 2.342 | 2.356 | −1252 | 9 | 6936 | 7235 | 1178 | 1 |
| 084401.95+050357.9 | ⋯ | 3.340 | ⋯ | 16 | 4458 | 8972 | 9558 | 3 |
| 084729.52+441616.7 | 2.347 | 2.344 | 269 | 16 | 1274 | 572 | 1785 | 1 |
| 085046.17+522057.4 | 2.230 | 2.234 | −371 | ⋯ | ⋯ | 1065 | 1641 | 3 |
| 091301.01+422344.7 | 2.315 | 2.314 | 91 | 59 | 1563 | 645 | 980 | 1 |
| 091328.23+394443.9 | ⋯ | 1.587 | ⋯ | ⋯ | ⋯ | 390 | 508 | 3 |
| 091425.72+504854.9 | 2.345 | 2.369 | −2493 | 28 | 1171 | 3817 | 7286 | 1 |
| 091716.79+461435.3 | ⋯ | 1.625 | ⋯ | ⋯ | ⋯ | 0 | 216 | 3 |
| 093251.98+023727.0 | 2.165 | 2.170 | −473 | 37 | 1928 | 4436 | 6935 | 1 |
| 094328.94+140415.6 | 2.430 | 2.408 | −704 | ⋯ | ⋯ | 0 | 1402 | 3 |
| 094427.27+614424.6 | 2.333 | 2.338 | −449 | 67 | 703 | 4169 | 6845 | 1 |
| 094902.38+531241.5 | 1.611 | 1.609 | 230 | 49 | 2502 | 753 | 2368 | 1 |
| 095746.75+565800.7 | 1.575 | 1.576 | −117 | 45 | 2925 | 808 | 0 | 2 |
| 100610.55+370513.8 | 3.204 | 3.202 | 143 | 53 | 1607 | 1441 | 1567 | 1 |
| 100653.26+011938.7 | 2.298 | 2.303 | −454 | 37 | 2382 | 6190 | 6715 | 1 |
| 101542.04+430455.6 | 2.364 | 2.417 | 702 | 13 | 4704 | 383 | 2079 | 1 |
| 102154.00+051646.3 | 3.439 | 3.448 | −607 | 24 | 2853 | 9177 | 1230 | 1 |
| 103246.19+323618.0 | 2.380 | 2.379 | 89 | 11 | 5562 | 4393 | 5752 | 3 |
| 103405.73+463545.4 | 2.215 | 2.215 | <\|90\| | 32 | 1816 | 0 | 699 | 1 |
| 103718.23+302509.1 | 2.293 | 2.288 | 456 | 44 | 1315 | 252 | 931 | 1 |
| 104621.57+483322.7 | ⋯ | 1.580 | ⋯ | ⋯ | ⋯ | 1676 | 2547 | 3 |
| 104941.58+522348.9 | ⋯ | 2.364 | ⋯ | 50 | 736 | 934 | 3557 | 3 |
| 110148.85+054815.5 | ⋯ | 1.584 | ⋯ | ⋯ | ⋯ | 0 | 1709 | 3 |
| 111313.29+102212.4 | 2.261 | 2.259 | 184 | 28 | 2349 | 613 | 1381 | 1 |
| 111352.53+104041.9 | ⋯ | 1.609 | ⋯ | ⋯ | ⋯ | 0 | 1939 | 3 |
| 111920.98+232539.4 | 2.289 | 2.289 | <\|90\| | 57 | 547 | 220 | 1907 | 3 |
| 112127.79+254758.9 | 1.587 | 1.601 | −1615 | 67 | 523 | 1008 | 3251 | 1 |
| 112938.46+440325.0 | 2.210 | 2.212 | 93 | ⋯ | ⋯ | 0 | 605 | 3 |
| 113048.45+225206.6 | 2.370 | 2.364 | 535 | 42 | 1782 | 6596 | 7168 | 1 |
| 113330.17+144758.8 | 3.252 | 3.242 | 424 | ⋯ | ⋯ | 616 | 1940 | 3 |
| 113740.61+630256.9 | 2.322 | 2.323 | −90 | 52 | 1408 | 5169 | 5889 | 3 |
| 113924.64+332436.9 | 2.314 | 2.315 | −91 | 28 | 3626 | 4283 | 5198 | 1 |
| 114323.71+193448.0 | 3.348 | 3.350 | −138 | 43 | 1308 | 0 | 1470 | 1 |
| 114705.24+083900.6 | 1.604 | 1.601 | 346 | ⋯ | ⋯ | 0 | 242 | 3 |
| 114738.35+301717.5 | 3.353 | 3.358 | −344 | 7 | 1574 | 0 | 336 | 1 |
| 115747.99+272459.6 | 2.206 | 2.216 | −933 | 32 | 1322 | 4076 | 5548 | 1 |
| 133342.56+123352.7 | 3.275 | 3.258 | 1198 | 20 | 2466 | 0 | 514 | 1 |
| 140058.79+260619.4 | 2.351 | 2.363 | −1071 | 37 | 1992 | 1851 | 2432 | 1 |
| 141321.05+092204.8 | 3.327 | 3.324 | 765 | 20 | 1734 | 58 | 964 | 1 |
| 142013.03+253403.9 | 2.235 | 2.235 | <\|90\| | 15 | 5255 | 2469 | 4993 | 1 |
| 142500.24+494729.2 | 2.260 | 2.261 | −92 | 15 | 3953 | 2648 | 3156 | 1 |
| 150205.58-024038.5 | ⋯ | 2.192 | ⋯ | 31 | 2774 | 6929 | 8100 | 3 |
| 151123.30+495101.2 | 2.380 | 2.379 | 265 | 19 | 4131 | 178 | 1954 | 1 |
| 151341.89+463002.7 | ⋯ | 1.572 | ⋯ | ⋯ | ⋯ | 2661 | 4651 | 3 |
| 153248.95+173900.8 | 2.350 | 2.350 | <\|90\| | 31 | 436 | 1437 | 4057 | 1 |
| 154550.37+554346.2 | 2.158 | 2.159 | −95 | 43 | 1050 | 0 | 350 | 3 |
| 160207.67+380743.0 | ⋯ | 1.581 | ⋯ | ⋯ | ⋯ | 0 | 0 | 4 |
| 160552.97+292141.4 | 2.321 | 2.333 | −1080 | 53 | 678 | 1767 | 3858 | 1 |
| 163125.10+174810.0 | 2.180 | 2.180 | <\|90\| | 20 | 1708 | 3042 | 5239 | 1 |
| 220344.98+235729.3 | ⋯ | 2.157 | ⋯ | 31 | −81 | 2170 | 3318 | 3 |

**Table 2**
(Continued)

| Quasar (SDSS J) | $z_{\rm vi}$[a] | $z_{\rm sys}$ | Velocity Offset (km $s^{-1}$) | $EW_{C IV}$[b] (Å) | $Blueshift_{C IV}$[b] (km $s^{-1}$) | BI (km $s^{-1}$) | AI (km $s^{-1}$) | BI/AI References[c] |
|---|---|---|---|---|---|---|---|---|
| 223934.45-004707.2 | 2.221 | 2.215 | 560 | 39 | 1040 | 110 | 349 | 1 |
| 225608.48+010557.8 | 2.268 | 2.263 | 460 | 40 | 1814 | 1217 | 3993 | 1 |

**Notes.**
[a] Value based on the visually inspected redshift measurement in SDSS DR16 (Lyke et al. 2020, Table D1, Column (17)) for 52 BAL quasars.
[b] Data taken from R20 for 52 GNIRS-DQS BAL quasars that appeared in their sample.
[c] References for the balnicity index and absorption index: (1) Paris et al. 2017; (2) Pâris et al. 2018; (3) Lyke et al. 2020; (4) Matthews et al. 2021; (5) Abazajian et al. 2009.

**Table 3**
BAL and Non-BAL Quasar Property Statistics and Comparisons

| Property | $\mu_{\rm BAL}$ | $\mu_{\rm non-BAL}$ | $SEM_{\rm BAL}$ | $SEM_{\rm non-BAL}$ | $\sigma_{\rm BAL}$ | $\sigma_{\rm non-BAL}$ | $Med_{\rm BAL}$ | $Med_{\rm non-BAL}$ | A-D $p$-value | K-S $p$-value |
|---|---|---|---|---|---|---|---|---|---|---|
| log $EW_{H\beta}$ | 1.77 | 1.77 | 0.02 | 0.01 | 0.16 | 0.14 | 1.79 ± 0.36 | 1.79 ± 0.24 | 0.25 | 0.84 |
| log $EW_{[O III]}$ | 1.19 | 1.14 | 0.04 | 0.03 | 0.33 | 0.35 | 1.22 ± 0.23 | 1.17 ± 0.17 | 0.25 | 0.69 |
| log $FWHM_{H\beta}$ | 3.68 | 3.63 | 0.02 | 0.01 | 0.12 | 0.13 | 3.68 ± 2.21 | 3.62 ± 1.98 | **0.002** | 0.11 |
| log $FWHM_{[O III]}$ | 3.19 | 3.14 | 0.04 | 0.03 | 0.02 | 0.24 | 0.26 | 3.23 ± 0.04 | 3.22 ± 0.03 | 0.25 |
| $Asymmetry_{[O III]}$ | −0.14 | −0.20 | 0.04 | 0.03 | 0.29 | 0.32 | −0.13 ± 0.06 | −0.20 ± 0.03 | 0.23 | 0.14 |
| $R_{Fe II}$ | 0.55 | 0.54 | 0.05 | 0.03 | 0.40 | 0.39 | 0.44 ± 0.05 | 0.48 ± 0.04 | 0.25 | 0.86 |
| log $M_{\rm BH}$ | 9.42 | 9.30 | 0.04 | 0.02 | 0.34 | 0.33 | 9.46 ± 0.04 | 9.29 ± 0.03 | **0.004** | 0.19 |
| $L/L_{\rm Edd}$ | 1.00 | 1.23 | 0.15 | 0.11 | 1.22 | 1.50 | 0.74 ± 0.06 | 1.04 ± 0.08 | 0.02 | 0.18 |
| Velocity offset [O III] (km $s^{-1}$) | 353.85 | 325.16 | 79.92 | 38.26 | 576.38 | 495.86 | 283.99 ± 112.77 | 308.38 ± 35.10 | 0.18 | 0.29 |
| Velocity offset ($z_{\rm vi} - z_{\rm sys}$) (km $s^{-1}$) | −224.41 | −226.60 | 133.06 | 68.86 | 959.50 | 840.56 | −90.39 ± 72.70 | −92.19 ± 61.71 | 0.25 | 0.98 |

**Note.** A comparison of several BAL and non-BAL spectral properties with probabilities of test statistics (see Section 3). The $p$-values highlighted in bold indicate rejection of null hypothesis at the 95% and 99% significance level.

Using the EWs of the Fe II blend and H$\beta$ line of all GNIRS-DQS quasars, a comparison is made between $R_{\rm Fe II}$, defined as EW(Fe II)/EW(H$\beta$), of BAL and non-BAL quasars as shown in Figure 1. The mean and median $R_{\rm Fe II}$ values for BAL and non-BAL quasars are consistent within their errors (see Table 3). This result indicates that BAL and non-BAL quasars, in this sample of highly luminous sources, have similar $L/L_{\rm Edd}$ distributions despite the presence of outflows in the former.

A similar comparison was performed between the FWHM values of the H$\beta$ line for the BAL and non-BAL quasars and is displayed in Figure 1. The figure also compares the $M_{\rm BH}$ values, which show a similar distribution to the FWHM (H$\beta$) distribution, as the $M_{\rm BH}$ values depend primarily on FWHM(H$\beta$) for sources in a relatively narrow luminosity range (e.g., D23). The comparison of the Eddington ratios ($L/L_{\rm Edd,}$where $L$ is the bolometric luminosity), both obtained from M23 and H23, for our populations of BAL and non-BAL quasars, presented in Figure 1, shows no significant differences between the two groups of sources. Figure 2 shows a correlation between $R_{\rm Fe II}$ and $L/L_{\rm Edd}$ values for the GNIRS-DQS BAL and non-BAL quasars. We find a Spearman rank correlation coefficient of 0.54 ($p = 3.48 \times 10^{-6}$) and 0.35 ($p = 4.58 \times 10^{-7}$) for BAL and non-BAL quasars, respectively. Both groups exhibit a statistically significant positive correlation between $R_{\rm Fe II}$ and $L/L_{\rm Edd}$.

To test whether the rest-frame optical properties of BAL quasars are significantly different from their non-BAL counterparts, we ran a two-tailed Kolmogorov–Smirnov (K-S) test on all the parameter distributions shown in Figure 1. We choose a cutoff for "significant" differences in distributions of $p = 0.05$ and $p = 0.01$ to indicate rejection or failure of rejection of the null hypothesis at the 95% and 99% significance level, respectively. Test results with $p$-values lower than these limits are possibly indicative of different parent populations for BAL quasars and non-BAL quasars, and they are highlighted in bold in Table 3.

To run the K-S test on the distributions of EW([O III]), we removed 13 BAL quasars and 27 non-BAL quasars that did not meet the M23 threshold of reliability for EW([O III]) values greater than 1 Å. In each test the hypothesis that properties from both samples, BAL and non-BAL quasars, arise from the same parent population could not be rejected at a significance level of 95% or 99% (see Table 3).

The K-S test may not effectively capture discrepancies in the tails of distributions. To address this issue, we also conducted a two-tailed Anderson–Darling (A-D) test on all the parameter distributions depicted in Figure 1, utilizing the same significance levels as employed in the K-S test. The A-D test exhibits greater sensitivity to differences in the tails of distributions and is capable of detecting even minute distinctions, particularly in large sample sizes. Our findings

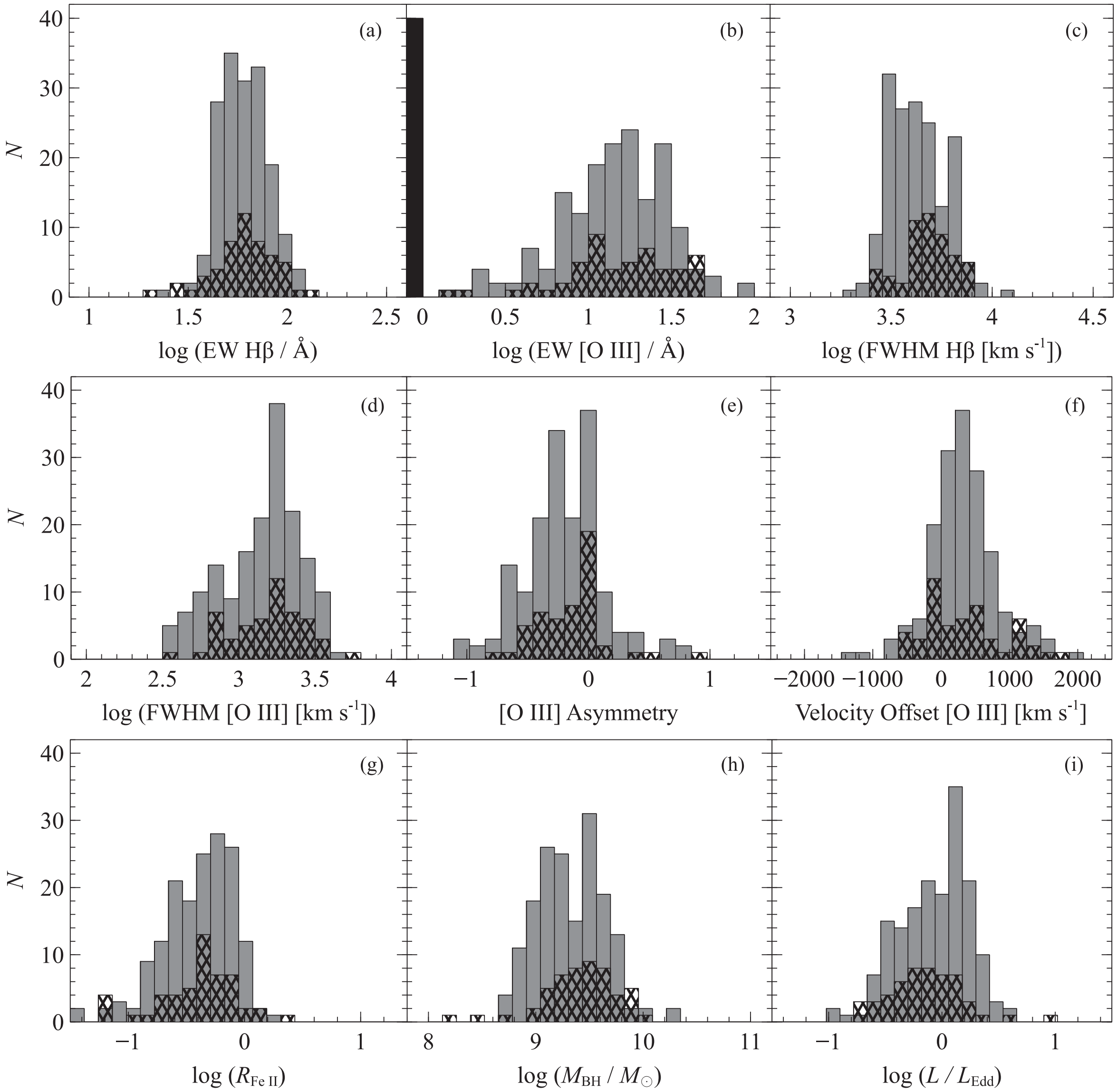

**Figure 1.** Distributions of the optical emission-line properties between BAL (hatched) and non-BAL (gray) quasars from the GNIRS-DQS sample. The comparison of all distributions reveals that the two populations are largely similar (see Section 3 and Table 3 for statistical analysis). For 40 sources (13 BAL and 27 non-BAL quasars) that did not meet the M23 threshold of reliability for an EW([O III]) measurement (i.e., greater than 1 Å); we place upper limits of 1 Å on their EW values (solid black column in panel (b); see also Table 1). The top row (panels (a), (b), and (c)) includes distributions of EW(H$\beta$), EW([O III]), and FWHM(H$\beta$) of 65 BAL and 195 non-BAL quasars. The middle row (panels (d), (e), and (f)) includes [O III] FWHM, asymmetry, and velocity offset distributions for only 52 BAL and 168 non-BAL quasars that meet the M23 EW([O iii]) threshold. The bottom row (panels (g), (h), and (i)) includes distributions of $R_{\text{Fe II}}$, $M_{\text{BH}}$, and $L/L_{\text{Edd}}$.

indicate that the null hypothesis, that both BAL and non-BAL quasars arise from the same parent population of sources, is rejected for FWHM(H$\beta$) and $M_{\text{BH}}$ at both the 95% and 99% significance levels and for $L/L_{\text{Edd}}$ at only the 95% significance level. However, the null hypothesis was not rejected at either significance level for EW(H$\beta$), EW([O III]), FWHM([O III]), asymmetry ([O III]), velocity offset ([O III]), or $R_{\text{Fe II}}$. In particular, we do not detect any manifestation of BAL outflows in the [O III] line properties of our sources.

We conducted a Monte Carlo simulation on properties where the null hypothesis was rejected with the A-D test, specifically focusing on $L/L_{\text{Edd}}$, $M_{\text{BH}}$, and FWHM(H$\beta$). In this simulation, we performed 10,000 realizations to account for uncertainties associated with each value. For approximately 90% of the 10,000 realizations, the A-D test was unable to reject the null hypothesis in each test. The simulation indicates that the A-D test is particularly sensitive to the tails of the distributions rather than the core values of $L/L_{\text{Edd}}$, $M_{\text{BH}}$, and FWHM(H$\beta$). Therefore, since each value carries a degree of uncertainty, it is important to interpret the A-D test results with caution.

If indeed $M_{\text{BH}}$, FWHM(H$\beta$), and possibly $L/L_{\text{Edd}}$ values of BAL and non-BAL quasars were found to originate from distinct parent populations, then this would have implied that the underlying mechanisms governing the broad-line region (BLR) dynamics and central SMBH accretion processes differ between these two groups of quasars. Any putative differences may have required refining mass estimation prescriptions to include additional BLR dynamics such as outflows. However, given that the differences are marginal at best, these properties remain broadly indistinguishable between BAL and non-BAL quasars.

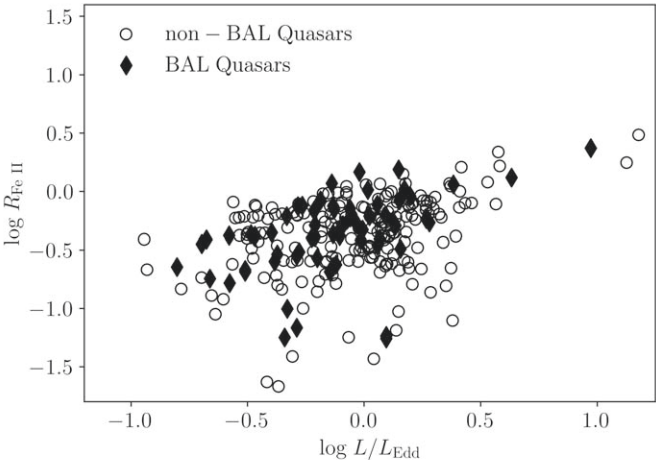

**Figure 2.** $R_{\rm Fe\,II}$ vs. $L/L_{\rm Edd}$ for non-BAL (open circles) quasars and BAL (diamonds) quasars from GNIRS-DQS. Both groups reveal a strong positive correlation between the two parameters (see Section 3.1).

### 3.2. Rest-frame UV Properties

To explore the C IV parameter space of BAL and non-BAL quasars, we compare a sample of 177 GNIRS-DQS non-BAL quasars with a sample of 52 BAL quasars with reliable C IV measurements taken from D23 and R20, respectively. D23 provides measurements of the C IV emission-line properties of 177 GNIRS-DQS sources, following the exclusion of 64 BAL quasars, 16 RL quasars, 1 BAL and RL quasar, and 2 sources that do not have reliable C IV coverage. For the BAL quasars, we adopted C IV measurements (EW and blueshift) from R20 for 52 of our sources (not including the single RL BAL quasar, SDSS J114705.24+083900.6) that appeared in their sample.

For a detailed description of the C IV measurements in our BAL quasars, we refer the reader to Section 6.1 of R20. In summary, calculation of the C IV emission-line parameters followed a nonparametric approach. Initially, a power-law continuum was subtracted from a reconstructed spectrum, after which the emission-line flux was integrated to determine the EW, and the blueshift was calculated from the wavelength that bisects the total cumulative line flux relative to the systemic redshift of the quasar. Wavelength regions of the spectra affected by BAL troughs were masked, covering areas blueward of the C IV emission line (i.e., 1430–1546 Å), resulting in a relatively symmetric emission-line profile.

The left panel of Figure 3 displays normalized values of the C IV emission-line EW versus blueshift for the 177 non-BAL quasars compared to 52 BAL quasars from GNIRS-DQS. While these two parameters, on their own, are not ideal accretion rate indicators (e.g., Richards et al. 2011; Shemmer & Lieber 2015), a combination of these two parameters appears to provide a robust indication of the accretion rate for all quasars as manifested in the right panel of Figure 3 (e.g., H23). This consolidated C IV parameterization, termed the C IV || Distance, indicates the projected location onto a nonlinear first principal component of the EW−blueshift diagram, and the piecewise polynomial best-fit curve traces the C IV parameter space of sources across wide ranges of redshifts and luminosities. To calculate the C IV || Distance parameter, we follow the procedure summarized in Rivera et al. (2022) and detailed in Richards et al. (2021).

Upon inspection of Figure 3, it appears that while BAL and non-BAL quasars demonstrate broad similarities within the C IV parameter space, the former tend to concentrate toward the top right above the best-fit curve in the left panel. We quantitatively tested this observation by also comparing the C IV ⊥ Distance parameter (the perpendicular to the C IV || Distance parameter), also defined in Rivera et al. (2022), between BAL and non-BAL quasars using a K-S test. The C IV ⊥ Distance parameter was measured relative to the closest (projected) point on the best-fit curve. The results indicate that the null hypothesis, that BAL and non-BAL quasars arise from the same parent population, can be rejected at significance levels of 95% and 99%. We suspect that this distinction between BAL and non-BAL quasars stems from the fact that measurements for the BAL quasars were performed by R20, while those for the non-BAL quasars were performed by D23, relying on $z_{\rm sys}$ values from M23.

In the case of C IV || Distance versus $L/L_{\rm Edd}$, we find a Spearman rank correlation coefficient of 0.52 ($p = 7.65 \times 10^{-5}$) and 0.28 ($p = 1.47 \times 10^{-4}$) for BAL and non-BAL quasars, respectively. This result indicates that, despite being a smaller subset of sources with potentially large uncertainties in the C IV measurements, the BAL quasars exhibit a stronger H$\beta$-based $L/L_{\rm Edd}$ and C IV || Distance correlation compared to non-BAL quasars. We fit a linear model to the C IV || Distance parameter and $L/L_{\rm Edd}$ space, taking into account only the non-BAL quasars. The mean deviation of the BAL quasars from the best-fit line is $\sim 1.05\sigma$.

We also searched for any potential relationship of BI and AI as a function of EW([O III]) and $L/L_{\rm Edd}$ values. However, we could not identify any significant correlation or trend among these parameters. We further performed an investigation of trough properties, including maximum and minimum velocity of each trough ($V_{\rm max}$, $V_{\rm min}$) and width of each trough ($V_{\rm width}$), as a function of H$\beta$-based $L/L_{\rm Edd}$ and $M_{\rm BH}$. The trough values were taken from R20 (see Table 1 therein) for 52 of our BAL sources that were part of their significantly larger sample. Our analysis does not reveal any significant correlation or discernible trend between the BAL trough properties and $L/L_{\rm Edd}$ or $M_{\rm BH}$. This lack of clear trend could be attributed to the constraints imposed by a small sample size and limitations inherent in deriving comprehensive information from basic measurements such as those obtained from R20 (see also Leighly et al. 2022).

To test whether BAL quasars exhibit significantly different blueshifts compared to non-BAL quasars, we compute the $\Delta v$ values between the $z_{\rm vi}$ value from Lyke et al. (2020)[15] and the $z_{\rm sys}$ value of a source taken from M23. If there is a noticeable difference, it could suggest the presence of an additional factor that is responsible for driving outflows in BAL quasars. The velocity offset is computed using

$$\Delta v = c\left(\frac{z_{\rm vi} - z_{\rm sys}}{1 + z_{\rm sys}}\right), \quad (3)$$

in a similar manner to Equation (3) in Section 3.1. The distributions of $\Delta v$ values for 52 BAL and 150 non-BAL quasars are presented in Figure 4; the $\Delta v$ values for the former[16] are taken from Table 2, and the $\Delta v$ values for the

---

[15] We note that for 20% of our BAL quasars the SDSS pipeline fails to provide a reliable redshift (Lyke et al. 2020, Table D1, Column (29)); thus, the $z_{\rm vi}$ values should be adopted. Lyke et al. (2020) only provide $z_{\rm vi}$ values for 52 BAL and 150 non-BAL GNIRS-DQS quasars (note that these 52 sources do not entirely coincide with the 52 sources that have C IV measurements in R20).

[16] The $z_{\rm vi}$ values of five of the sources are identical to their $z_{\rm sys}$ values. We, therefore, assign an upper limit of |90| km s$^{-1}$ for their $\Delta v$ values in Table 2; these values are treated as zeros in Figure 4 and our analysis.

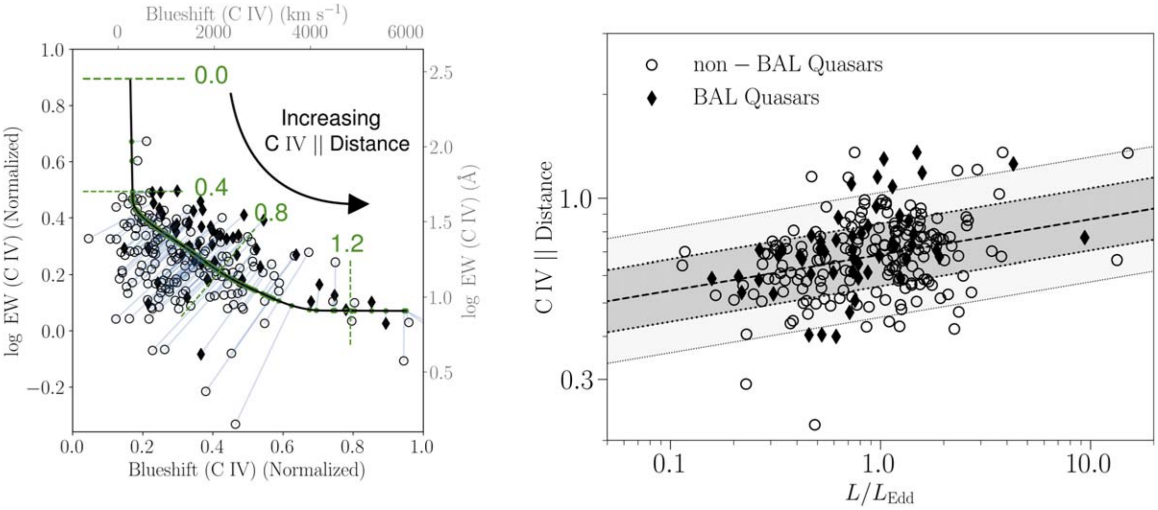

**Figure 3.** Left panel: distribution of EW(C IV) vs. blueshift (C IV) for 177 non-BAL quasars and 52 BAL quasars; symbols are the same as in Figure 2. The data are first normalized so that the two axes share the same limit; each data point is then projected (thin blue lines) onto the best-fit curve obtained from Rivera et al. (2022). The C IV || Distance value of each quasar is defined as its projected position (green point) along the solid black curve. Representative C IV || Distance values are indicated by dashed lines and numbers. The ranges of C IV blueshift and EW are −1000–6000 km s$^{-1}$ and 2–140 Å, respectively. Right panel: C IV || Distance parameter vs. Fe II−corrected H$\beta$-based $L/L_{\rm Edd}$. The correlation for the non-BAL quasar sample, obtained by fitting a linear model, is indicated by a dashed line. The dark (light) shaded region represents the 1$\sigma$ (2$\sigma$) deviation from the fitted correlation (see Section 3).

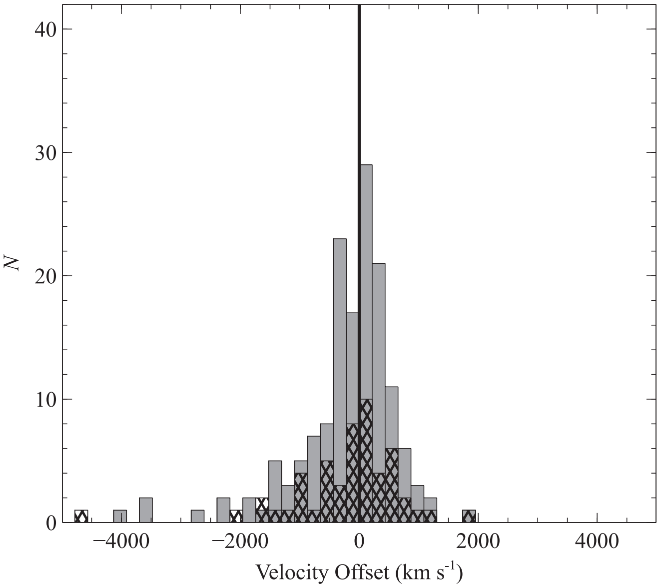

**Figure 4.** Distribution of the velocity offset between $z_{\rm vi}$ from Lyke et al. (2020) and the $z_{\rm sys}$ value of a source between BAL (hatched) and non-BAL (gray) quasars from the GNIRS-DQS sample. The zero velocity offset is indicated by the solid line. Based on statistical tests, both distributions are broadly similar (see Section 3).

latter are computed using $z_{\rm vi}$ values from Lyke et al. (2020) and $z_{\rm sys}$ values from M23.

The comparison of both distributions of BAL and non-BAL quasars reveals no significant difference between these two populations. We confirm this result by running K-S and A-D tests on the distributions in a similar manner to the tests run in Section 3.1. Our analysis reveals that the hypothesis asserting that $\Delta v$ from both samples, BAL and non-BAL quasars, come from the same parent population was not rejected at the 95% or 99% significance level with the K-S and A-D tests (see Table 3). This result highlights the fact that both populations exhibit a high degree of similarity.

## 4. Discussion

We find that BAL quasars are generally indistinguishable from their non-BAL counterparts in the rest-frame optical band, an extension of the W91 result concerning rest-frame UV emission-line properties. This conclusion resonates with the results of Schulze et al. (2017), who find no discernible differences in the rest-frame optical properties between LoBAL and non-BAL quasars, particularly with respect to their $M_{\rm BH}$ and $L/L_{\rm Edd}$ values. To understand the underlying causes behind the appearance of BAL troughs in quasar spectra, we consider the potential influence of accretion rate and orientation.

Our highly uniform sample consists of quasars selected at high redshifts with high luminosities, likely above the luminosity threshold required to launch accretion disk winds (e.g., Laor & Brandt 2002; Bieri et al. 2017; Quera-Bofarull et al. 2023). Giustini & Proga (2019) further argue that the strongest winds are expected to arise in objects with both the highest $M_{\rm BH}$ values and the highest accretion rates, such as those in the GNIRS-DQS sample (see also D23; Temple et al. 2023). This may explain the relatively high fraction of BAL quasars observed in GNIRS-DQS.

Figure 5 depicts how the observed BAL quasar fraction in GNIRS-DQS changes as a function of luminosity. For comparison, Figure 5 also displays similar data for SDSS DR16 quasars, which is the parent sample of the GNIRS-DQS sources. For this comparison sample, we only included sources identified in Lyke et al. (2020) as having a BAL probability $\geqslant$0.75. We further limited that sample to sources lying in the redshift ranges $1.57 \leqslant z \lesssim 1.65$, $2.10 \lesssim z \lesssim 2.40$, and $3.20 \lesssim z \lesssim 3.50$, similar to the GNIRS-DQS redshift intervals; no brightness restriction was applied. Since SDSS DR16 only identifies BAL quasars at $z \geqslant 1.57$, two GNIRS-DQS sources are excluded from Figure 5, SDSS J080636.81 + 345048.5 at $z = 1.553$ and SDSS J090247.57 + 304120.7 at $z = 1.560$. For all sources in Figure 5, monochromatic luminosities at a rest-frame wavelength of 2500 Å were derived from the point-spread function $m_i$ values in Lyke et al. (2020), assuming a

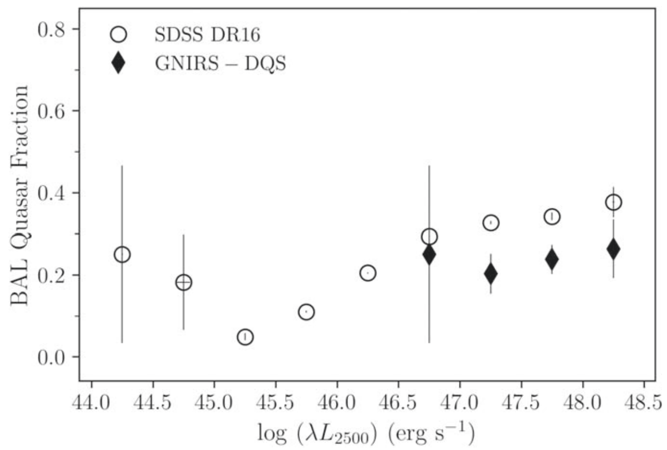

**Figure 5.** Fraction of BAL quasars as a function of $\lambda L_\lambda$ at 2500 Å. Each point represents the average BAL quasar fraction within equal luminosity bins ($\Delta\lambda L_\lambda$) of 0.5 dex. The SDSS DR16 sample (Lyke et al. 2020) includes 141,241 quasars between $1.57 \leqslant z \lesssim 3.5$.

quasar continuum of the form $f_\nu \propto \nu^{-0.5}$ (e.g., Vanden Berk et al. 2001). These luminosities are represented by equal bins of $(\Delta\lambda L_\lambda) = 0.5$ dex, including ∼4–60,000 sources per bin, with error bars representing the SEM of the BAL fraction in each bin.

According to Figure 5, it appears as if the BAL fraction increases as a function of luminosity. It is also apparent that the BAL fractions of the GNIRS-DQS sources are generally consistent with those of their parent SDSS sample. This trend of increasing BAL fraction as a function of luminosity is also broadly consistent with the results of Ganguly et al. (2007b). A different approach employed by Allen et al. (2011) for SDSS quasars reports intrinsic BAL quasar fractions that are somewhat larger than the values we derive from the Lyke et al. (2020) sample at higher luminosities. The Allen et al. (2011) data can be considered as conservative upper limits to the BAL quasar fractions for luminous quasars. As indicated by Laor & Brandt (2002) and Ganguly & Brotherton (2008), quasars with low luminosity ($\lambda L_\lambda \lesssim 10^{44}$ erg s$^{-1}$) are not capable of attaining the requisite high maximum velocity of the outflow necessary for the manifestation of the BAL phenomenon according to the W91 definition. This trend is consistent with the data in Figure 5.

Instead of the increased ability to launch outflows as luminosity increases, there are alternative explanations to the observed trend of increased BAL fraction as a function of luminosity. For example, Yuan & Wills (2003) argue that the trend of increasing BAL fraction with increasing luminosity could be a consequence of low-luminosity sources having a shortage of gas supply and hence lower Eddington ratios. Therefore, sources that have the largest supply of cold gas (at higher redshifts) have the largest fueling and outflow rates and exhibit BAL troughs. Another explanation for this trend may be related to low-luminosity quasars typically having low-S/N spectra, in which a BAL trough is less likely to be identified as such (e.g., Allen et al. 2011, R20).

At lower redshifts ($z \lesssim 1.5$), the characterization of BAL quasars remains unclear, primarily due to the scarcity of available rest-frame UV data, as the majority of BAL quasar studies lack a statistically significant number of sources. For example, Brandt et al. (2000) report five BAL quasars out of a sample of 87 sources. Similarly, the Ganguly et al. (2007a) sample includes two BAL quasars out of 14 sources, and the Matthews et al. (2017) sample has 58 BAL quasars out of 16,742 sources, though their sample consists exclusively of LoBAL quasars. Moreover, since luminous quasars lie preferentially at higher redshifts and the BAL quasar fraction decreases toward lower luminosities, the census of nearby BAL quasar targets is quite limited.

Another factor that may contribute to the observation of BAL troughs in quasar spectra is orientation. The outflows in BAL quasars may not be directed along our line of sight, which might potentially account for the observed BAL fraction of 10%–15% at viewing angles less than ∼30° relative to the plane of the disk within the larger population of quasars (e.g., Zhou et al. 2006; DiPompeo et al. 2012). An additional complication that arises is that quasars viewed at angles above 45° (more edge-on) are likely obscured by dust (e.g., Barthel 1989).

Nair & Vivek (2022) observe that the BAL quasar sample at high orientation angles is almost double the BAL quasar fraction at low orientation angles (∼40% compared to ∼20%), pointing to the possible existence of polar BAL quasars. Kunert-Bajraszewska et al. (2015) also found that stronger C IV absorption is associated with lower values of the radio-loudness parameter, and thus with high orientation angles for BAL quasars. This trend is consistent with our GNIRS-DQS sample of 65 BAL quasars, only one of which is also RL (see Section 2), constituting a considerably lower fraction of RL sources among the general quasar population. This observation supports the idea that BAL quasars tend to occupy large orientation angles. Similar findings by DiPompeo et al. (2012) indicate a general trend suggesting that BAL quasar viewing angles extend about 10° farther from the radio jet axis.

Figure 5 indicates that a certain threshold luminosity, $\lambda L_{2500} \gtrsim 10^{45}$ erg s$^{-1}$, is a necessary condition for the production of outflows. While high luminosity is required, it is clearly insufficient to guarantee the appearance of a BAL trough. Even in the most luminous quasars, the BAL fraction remains below ∼40% (see Figure 5; but see also Figure 28 of Allen et al. 2011 for a somewhat larger intrinsic BAL fraction). This trend can be explained by a limited BAL covering fraction observed at preferential orientation angles. All this suggests that orientation plays a significant role in the appearance of BAL troughs in quasar spectra (see also Filiz et al. 2013; Filiz & Brandt 2014).

By design, GNIRS-DQS encompasses only high luminosity, and consequently high $M_{\rm BH}$ values, providing limited insights into the properties of BAL quasars across the broader quasar parameter space (see M21; Figure 5). Extending GNIRS-DQS to lower luminosities would allow inclusion of distant sources with lower $M_{\rm BH}$ values, enabling one to disentangle the roles that luminosity, $M_{\rm BH}$, and orientation play in the appearance of BAL troughs in quasar spectra. This goal could be achieved most efficiently by employing NIR spectrographs on future large observatories such as the European Extremely Large Telescope (e.g., Thatte et al. 2016), the Giant Magellan Telescope (e.g., Jaffe et al. 2016), or the Thirty Meter Telescope (e.g., Larkin et al. 2016).

## 5. Summary and Conclusions

In this work, we conduct a comparative analysis of the rest-frame optical properties of 65 BAL quasars and 195 non-BAL quasars to gain insights into the appearance of BAL features in quasar spectra. All the quasars were drawn from GNIRS-DQS, a flux-limited uniform sample of luminous sources at $1.55 \lesssim z \lesssim 3.50$ that have spectroscopic data of the H$\beta$ region. Our BAL quasar sample, which constitutes a BAL quasar fraction of 25%, is the largest uniform sample of such sources having rest-frame optical spectral properties. We perform careful comparisons between BAL quasars and non-BAL quasars based on velocity offsets from systemic redshifts and emission-line properties, such as EW, FWHM, and $R_{\text{Fe II}}$. We also explore correlations between BAL trough properties and the H$\beta$-based SMBH masses and normalized accretion rates.

We find that, in spite of the differences between luminous BAL and non-BAL quasars in their rest-frame UV spectra, they are generally indistinguishable in their rest-frame optical spectra. This result is broadly consistent with the idea that the BALs observed in the rest-frame UV spectra of luminous quasars are the result of clumpy, outflowing gas along the line of sight (e.g., W91; Yong et al. 2018). Specifically, all luminous quasars have the potential to be seen as BAL quasars, but the appearance of BAL features may depend on the orientation of the outflow with respect to our line of sight. We do not find any significant correlations between BAL trough properties and either $M_{\text{BH}}$ or $L/L_{\text{Edd}}$ in our sample, and, overall, the velocity offsets from systemic redshifts of our BAL quasars are similar to their non-BAL counterparts. A future extension of the high-redshift sample to considerably lower luminosities may allow one to explore the contributions of luminosity, $M_{\text{BH}}$, and orientation to the quasar BAL phenomenon.

## Acknowledgments

This work is supported by National Science Foundation (NSF) grants AST-1815281 (H.A., B.M.M., C.D., O.S.) and AST-1815645 (M.S.B., A.D.M., J.N.M.). We thank an anonymous reviewer for valuable comments that helped improve this manuscript. This research has made use of the NASA/IPAC Extragalactic Database (NED), which is operated by the Jet Propulsion Laboratory, California Institute of Technology, under contract with the National Aeronautics and Space Administration. T.H. acknowledges support from a predoctoral program at the Flatiron Institute. Research at the Flatiron Institute is supported by the Simons Foundation.

*Software:* MATLAB and Statistics Toolbox (MATLAB 2022), matplotlib (Hunter 2007), numpy (van der Walt et al. 2011); (Harris et al. 2020), pandas (McKinney 2010), scipy (Virtanen et al. 2020), scikit-learn (Pedregosa et al. 2011).

## ORCID iDs

Harum Ahmed https://orcid.org/0009-0008-0969-4084
Ohad Shemmer https://orcid.org/0000-0003-4327-1460
Brandon Matthews https://orcid.org/0000-0001-8406-4084
Cooper Dix https://orcid.org/0000-0003-0192-1840
Trung Ha https://orcid.org/0000-0001-6600-2517
Gordon T. Richards https://orcid.org/0000-0002-1061-1804
Michael S. Brotherton https://orcid.org/0000-0002-1207-0909
W. N. Brandt https://orcid.org/0000-0002-0167-2453
Sarah C. Gallagher https://orcid.org/0000-0001-6217-8101
Richard Green https://orcid.org/0000-0003-1245-5232
Paulina Lira https://orcid.org/0000-0003-1523-9164
Jacob N. McLane https://orcid.org/0000-0003-1081-2929
Richard M. Plotkin https://orcid.org/0000-0002-7092-0326
Donald P. Schneider https://orcid.org/0000-0001-7240-7449

## References

Abazajian, K. N., Adelman-McCarthy, J. K., Agüeros, M. A., et al. 2009, ApJS, 182, 543
Allen, J. T., Hewett, P. C., Maddox, N., Richards, G. T., & Belokurov, V. 2011, MNRAS, 410, 860
Baldwin, J. A. 1977, ApJ, 214, 679
Barthel, P. D. 1989, ApJ, 336, 606
Baskin, A., Laor, A., & Hamann, F. 2013, MNRAS, 432, 1525
Becker, R. H., Gregg, M. D., Hook, I. M., et al. 1997, ApJL, 479, L93
Becker, R. H., White, R. L., Gregg, M. D., et al. 2001, ApJS, 135, 227
Begelman, M. C., Volonteri, M., & Rees, M. J. 2006, MNRAS, 370, 289
Bieri, R., Dubois, Y., Rosdahl, J., et al. 2017, MNRAS, 464, 1854
Boroson, T. A., & Green, R. F. 1992, ApJS, 80, 109
Boroson, T. 2005, AJ, 130, 381
Brandt, W. N., Laor, A., & Wills, B. J. 2000, ApJ, 528, 637
Brotherton, M. S., van Breugel, W., Smith, R. J., et al. 1998, ApJL, 505, L7
Brotherton, M. S., De Breuck, C., & Schaefer, J. J. 2006, MNRAS, 372, L58
Calistro Rivera, G., Alexander, D. M., Harrison, C. M., et al. 2023, arXiv:2312.10177
Cattaneo, A., Blaizot, J., Devriendt, J., & Guiderdoni, B. 2005, MNRAS, 364, 407
Di Matteo, T., Springel, V., & Hernquist, L. 2005, Natur, 433, 604
Dietrich, M., Hamann, F., Shields, J. C., et al. 2002, ApJ, 581, 912
DiPompeo, M. A., Brotherton, M. S., & De Breuck, C. 2012, ApJ, 752, 6
DiPompeo, M. A., Myers, A. D., Brotherton, M. S., Runnoe, J. C., & Green, R. F. 2014, ApJ, 787, 73
Dix, C., Matthews, B., Shemmer, O., et al. 2023, ApJ, 950, 96
Du, P., & Wang, J.-M. 2019, ApJ, 886, 42
Elvis, M. 2000, ApJ, 545, 63
Filiz, A. N., Brandt, W. N., Hall, P. B., et al. 2013, ApJ, 777, 168
Filiz, A. N., Brandt, W. N., & Hall, P. B. 2014, ApJ, 791, 88
Gallagher, S. C., Brandt, W. N., Chartas, G., & Garmire, G. P. 2002, ApJ, 567, 37
Gallagher, S. C., Brandt, W. N., Chartas, G., et al. 2006, ApJ, 644, 709
Gallagher, S. C., Hines, D. C., Blaylock, M., et al. 2007, ApJ, 665, 157
Ganguly, R., Brotherton, M. S., Arav, N., et al. 2007a, AJ, 133, 479
Ganguly, R., Brotherton, M. S., Cales, S., et al. 2007b, ApJ, 665, 990
Ganguly, R., & Brotherton, M. S. 2008, ApJ, 672, 102
García, L. Á, Martini, P., Gonzalez-Morales, A. X., et al. 2023, MNRAS, 526, 4848
Gibson, R. R., Jiang, L., Brandt, W. N., et al. 2009, ApJ, 692, 758
Giustini, M., & Proga, D. 2019, A&A, 630, A94
Gregg, M. D., Becker, R. H., & de Vries, W. 2006, ApJ, 641, 210
Ha, T., Dix, C., Matthews, B. M., et al. 2023, ApJ, 950, 97
Hall, P. B., Anderson, S. F., Strauss, M. A., et al. 2002, ApJS, 141, 267
Harris, C. R., Millman, K. J., van der Walt, S. J., et al. 2020, Natur, 585, 357
Hopkins, P. F., Hernquist, L., Cox, T. J., et al. 2005, ApJ, 630, 705
Hu, J., Shen, Y., Lou, Y.-Q., & Zhang, S. 2006, MNRAS, 365, 345
Hunter, J. D. 2007, CSE, 9, 90
Jaffe, D. T., Barnes, S., Brooks, C., et al. 2016, Proc. SPIE, 9908, 990821
Kellermann, K. I., Sramek, R., Schmidt, M., Shaffer, D. B., & Green, R. 1989, AJ, 98, 1195
Knigge, C., Scaringi, S., Goad, M. R., & Cottis, C. E. 2008, MNRAS, 386, 1426
Kunert-Bajraszewska, M., Cegłowski, M., Katarzyński, K., & Roskowiński, C. 2015, A&A, 579, A109
Laor, A., & Brandt, W. N. 2002, ApJ, 569, 641
Larkin, J. E., Moore, A. M., Wright, S. A., et al. 2016, Proc. SPIE, 9908, 99081W
Leighly, K. M., Choi, H., DeFrancesco, C., et al. 2022, ApJ, 935, 92
Lípari, S. L., & Terlevich, R. J. 2006, MNRAS, 368, 1001
Liu, H., Luo, B., Brandt, W. N., Gallagher, S. C., & Garmire, G. P. 2018, ApJ, 859, 113
Luo, B., Brandt, W. N., Alexander, D. M., et al. 2014, ApJ, 794, 70
Lyke, B. W., Higley, A. N., McLane, J. N., et al. 2020, ApJS, 250, 8
Magorrian, J., Tremaine, S., Richstone, D., et al. 1998, AJ, 115, 2285
Maithil, J., Brotherton, M. S., Shemmer, O., et al. 2022, MNRAS, 515, 491
Marconi, A., & Hunt, L. K. 2003, ApJL, 589, L21
MATLAB 2022, v9.12.0 (R2022a) (Natick, MA: The MathWorks Inc.)
Matthews, B. M., Shemmer, O., Dix, C., et al. 2021, ApJS, 252, 15
Matthews, B. M., Dix, C., Shemmer, O., et al. 2023, ApJ, 950, 95
Matthews, J. H., Knigge, C., & Long, K. S. 2017, MNRAS, 467, 2571
McKinney, W. 2010, in Proc. of the 9th Python in Science Conf., ed. S. van der Walt & J. Millman (Austin, TX: SciPy), 56

Morabito, L. K., Dai, X., Leighly, K. M., Sivakoff, G. R., & Shankar, F. 2014, ApJ, 786, 58
Murray, N., Chiang, J., Grossman, S. A., & Voit, G. M. 1995, ApJ, 451, 498
Nair, A., & Vivek, M. 2022, MNRAS, 511, 4946
Netzer, H., Shemmer, O., Maiolino, R., et al. 2004, ApJ, 614, 558
Netzer, H., & Trakhtenbrot, B. 2007, ApJ, 654, 754
Nguyen, N. H., Lira, P., Trakhtenbrot, B., et al. 2020, ApJ, 895, 74
Ogle, P. M., Cohen, M. H., Miller, J. S., et al. 1999, ApJS, 125, 1
Pâris, I., Petitjean, P., Ross, N. P., et al. 2017, A&A, 597, A79
Pâris, I., Petitjean, P., Aubourg, É., et al. 2018, A&A, 613, A51
Pedregosa, F., Varoquaux, G., Gramfort, A., et al. 2011, JMLR, 12, 2825
Petley, J. W., Morabito, L. K., Rankine, A. L., et al. 2024, MNRAS, 529, 1995
Quera-Bofarull, A., Done, C., Lacey, C. G., Nomura, M., & Ohsuga, K. 2023, MNRAS, 518, 2693
Rankine, A. L., Hewett, P. C., Banerji, M., & Richards, G. T. 2020, MNRAS, 492, 4553
Reichard, T. A., Richards, G. T., Hall, P. B., et al. 2003, AJ, 126, 2594
Richards, G. T., Vanden Berk, D. E., Reichard, T. A., et al. 2002, AJ, 124, 1
Richards, G. T., Kruczek, N. E., Gallagher, S. C., et al. 2011, AJ, 141, 167
Richards, G. T., McCaffrey, T. V., Kimball, A., et al. 2021, AJ, 162, 270
Rivera, A. B., Richards, G. T., Gallagher, S. C., et al. 2022, ApJ, 931, 154
Runnoe, J. C., Shang, Z., & Brotherton, M. S. 2013, MNRAS, 435, 3251
Schmidt, G. D., & Hines, D. C. 1999, ApJ, 512, 125
Schulze, A., Schramm, M., Zuo, W., et al. 2017, ApJ, 848, 104
Shemmer, O., & Lieber, S. 2015, ApJ, 805, 124
Shen, Y., Brandt, W. N., Richards, G. T., et al. 2016, ApJ, 831, 7
Shen, Y., & Ho, L. C. 2014, Natur, 513, 210
Silk, J., & Rees, M. J. 1998, A&A, 331, L1
Spergel, D. N., Bean, R., Doré, O., et al. 2007, ApJS, 170, 377
Sprayberry, D., & Foltz, C. B. 1992, ApJ, 390, 39
Stocke, J. T., Morris, S. L., Weymann, R. J., & Foltz, C. B. 1992, ApJ, 396, 487
Temple, M. J., Matthews, J. H., Hewett, P. C., et al. 2023, MNRAS, 523, 646
Teng, S. H., Brandt, W. N., Harrison, F. A., et al. 2014, ApJ, 785, 19
Thatte, N. A., Clarke, F., Bryson, I., et al. 2016, Proc. SPIE, 9908, 99081X
Trump, J. R., Hall, P. B., Reichard, T. A., et al. 2006, ApJS, 165, 1
Urrutia, T., Becker, R. H., White, R. L., et al. 2009, ApJ, 698, 1095
van der Walt, S., Colbert, S. C., & Varoquaux, G. 2011, CSE, 13, 22
Vanden Berk, D. E., Richards, G. T., Bauer, A., et al. 2001, AJ, 122, 549
Virtanen, P., Gommers, R., Burovski, E., et al. 2020, NatMe, 17, 261
Voit, G. M., Weymann, R. J., & Korista, K. T. 1993, ApJ, 413, 95
Wang, C., Luo, B., Brandt, W. N., et al. 2022, ApJ, 936, 95
Weymann, R. J., Morris, S. L., Foltz, C. B., & Hewett, P. C. 1991, ApJ, 373, 23
Wright, E. L., Eisenhardt, P. R. M., Mainzer, A. K., et al. 2010, AJ, 140, 1868
Yang, G., Brandt, W. N., Vito, F., et al. 2018, MNRAS, 475, 1887
Yong, S. Y., King, A. L., Webster, R. L., et al. 2018, MNRAS, 479, 4153
York, D. G., Adelman, J., Anderson, J. E. J., et al. 2000, AJ, 120, 1579
Yuan, M. J., & Wills, B. J. 2003, ApJL, 593, L11
Zhou, H., Wang, T., Wang, H., et al. 2006, ApJ, 639, 716